Twinned calcite as an indicator of high differential stresses and low shock pressure conditions during impact cratering

Lina SEYBOLD [ID] [1,2]*, Claudia A. TREPMANN [ID] [1], Stefan HÖLZL [1,2], Kilian POLLOK [3], Falko LANGENHORST [3], Fabian DELLEFANT [1], and Melanie KALIWODA [1,4]

[1]Department of Earth and Environmental Sciences, Ludwig-Maximilians-University Munich, Munich, Germany
[2]Bavarian Natural History Collections, RiesKraterMuseum Nördlingen, Nördlingen, Germany
[3]Institute of Geoscience, Friedrich Schiller University Jena, Jena, Germany
[4]Mineralogical State Collection, Bavarian Natural History Collections, Munich, Germany
*Correspondence
Lina Seybold, Department of Earth and Environmental Sciences, Ludwig-Maximilians-University Munich, Luisenstr. 37, Munich 80333, Germany.
Email: lina.seybold@lmu.de

Abstract–Shock-related calcite twins are characterized in calcite-bearing metagranite cataclasites within crystalline megablocks of the Ries impact structure, Germany, as well as in cores from the FBN1973 research drilling. The calcite likely originates from pre-impact veins within the Variscan metagranites and gneisses, while the cataclasis is due to the Miocene impact. Quartz in the metagranite components does not contain planar deformation features, indicating low shock pressures (<7 GPa). Calcite, however, shows a high density (>1/μm) of twins with widths <100 nm. Different types of twins (*e*-, *f*-, and *r*-twins) crosscutting each other can occur in one grain. Interaction of *r*- and *f*-twins results in *a*-type domains characterized by a misorientation relative to the host with a misorientation angle of 35°–40° and a misorientation axis parallel to an *a*-axis. Such *a*-type domains have not been recorded from deformed rocks in nature before. The high twin density and activation of different twin systems in one grain require high differential stresses (on the order of 1 GPa). Twinning of calcite at high differential stresses is consistent with deformation during impact cratering at relatively low shock pressure conditions. The twinned calcite microstructure can serve as a valuable low shock barometer.

INTRODUCTION

Calcite is an important rock-forming mineral of the Earth's upper crust (e.g., in carbonates and marbles). Its rheological behavior is important for rapid crustal deformation processes, ranging from seismic faulting to impact cratering. Carbonates are present not only on Earth but also on Mars (e.g., Niles et al., 2013), in micrometeorites (Dobrică et al., 2022), carbonaceous chondrites (e.g., Grady et al., 1988; Lindgren et al., 2011; Lee et al., 2014), and their parent asteroids (Kaplan et al., 2020) and can potentially serve as useful recorders of deformation phenomena on other bodies in the solar system. Yet, the way carbonates respond to shock and behave during impact cratering is poorly constrained (e.g., Kurosawa et al., 2021, 2022; Stöffler et al., 2018 and references therein).

In tectonic settings, twinning is the dominant deformation mechanism of calcite at low temperatures (<300°C), relatively high strain rates (e.g., 10^{-4} s^{-1}), and ambient pressures sufficient to impede brittle deformation as studied in numerous deformation experiments (e.g., Barber & Wenk, 1979; De Bresser & Spiers, 1993, 1997; Parlangeau et al., 2019; Rowe & Rutter, 1990; Rybacki et al., 2013, 2021; Schuster et al., 2020). Mechanical twinning involves the generation and movement of partial
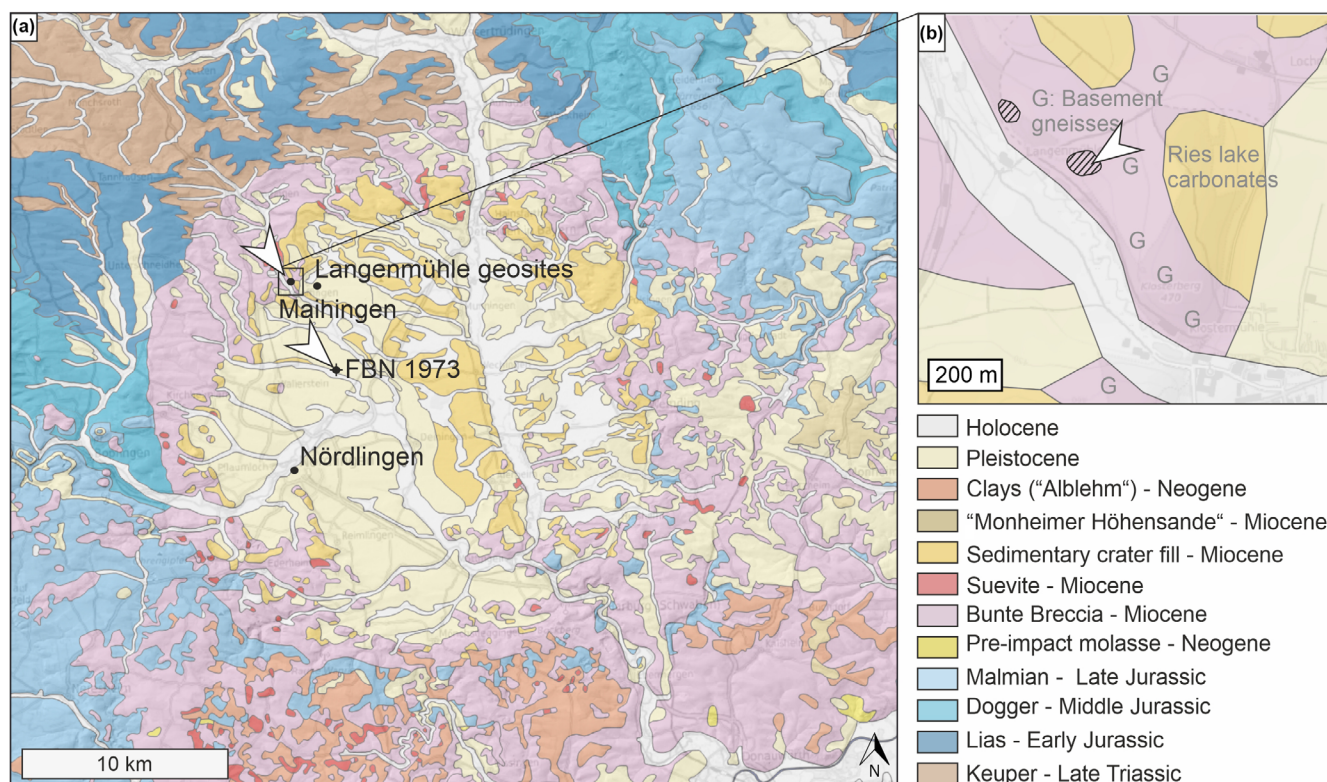
FIGURE 1. Geological maps of the Nördlinger Ries with white arrows marking the sample locations. (a) Overview with sample locations NW of Maihingen and the location of the 1973 research drilling (FBN1973). (b) Close up on the area NW of Maihingen, with outcrops marked as shaded areas and sample locations. Maps edited after: The General Geological Map of the Federal Republic of Germany 1:250,000 (GÜK250), © Bundesanstalt für Geowissenschaften und Rohstoffe (BGR). (Color figure can be viewed at wileyonlinelibrary.com)

dislocations upon shear stress and does not require thermally activated diffusion (Hirth & Lothe, 1982). It requires that a critical resolved shear stress is reached on the given twin plane in the given glide direction, which is for the known calcite twin systems several tens of MPa (e.g., Covey-Crump et al., 2017; Parlangeau et al., 2019). The resolved shear stress on a twin plane in the associated glide direction is dependent on the differential stress and the orientation of the twin plane and glide direction to the principal stress directions according to the Schmid formula:

$$\tau_{res} = \sigma_d \cdot \cos\gamma \cdot \cos\theta,$$

where τ_{res} is the resolved shear stress, σ_d is the differential stress, γ is the angle of the plane normal to the maximum principal stress direction, and θ is the angle of the glide direction to the maximum principal stress direction, the term $\cos\gamma \cdot \cos\theta$ is known as Schmid factor, which has an absolute maximum at 0.5. Thus, the activation of different twin systems is mostly

dependent on the differential stress, whereas strain rate, temperature, and confining pressures have been found to have only a minor effect (e.g., Parlangeau et al., 2019; Rowe & Rutter, 1990). In contrast, the broadening of twins requires thermally activated dislocation climb and therefore the twin morphology is dependent on temperature (Burkhard, 1993; Ferrill et al., 2004). Calcite twinning is well-known in tectonic fault rocks (e.g., Arboit et al., 2015; Burkhard, 1993; Lacombe, 2007), where it is commonly used for strain analyses (e.g., Craddock et al., 2022; Groshong Jr, 1972) and paleostress analyses during faulting (Lacombe, 2007 and references therein; Rybacki et al., 2013). Calcite twinning is rarely described from terrestrial impactites (Burt et al., 2005) and shock deformation experiments (Kenkmann et al., 2018; Kurosawa et al., 2022; Langenhorst et al., 2003; Lindgren et al., 2013).

The Ries impact structure is an ideal site to study calcite deformation during impact cratering, because the impactites are well preserved with no influence from subsequent tectonic deformation since the impact about 14.8 Ma ago (Rocholl, Böhme, et al., 2018; Rocholl,

Schaltegger, et al., 2018; Schmieder et al., 2018a, 2018b; Schwarz et al., 2020). In this study, we use the microfabrics of twinned calcite in calcite-bearing metagranite cataclasites within megablocks close to the peak ring of the Nördlinger Ries structure to identify the relevant deformation mechanisms (Figure 1). We compare our results with experimental observations from shock experiments (Langenhorst et al., 2003) and deformation experiments at high tectonic stresses and high strain rates (e.g., 10^{-4} s^{-1} Barber & Wenk, 1979; up to 1.7×10^{-2} s^{-1} Schuster et al., 2020) and use the twin width, density and spacing as a paleopiezometer (Rybacki et al., 2013). From the twinned microstructure, we obtain information on the deformation conditions, which is a prerequisite for a better understanding of calcite deformation during impact cratering.

THE RIES IMPACT STRUCTURE

The Ries is a complex impact structure with a diameter of about 26 km and was formed about 14.8 Ma ago in the middle Miocene (Rocholl, Böhme, et al., 2018; Rocholl, Schaltegger, et al., 2018; Schmieder et al., 2018a; Schwarz et al., 2020). The impact affected the sedimentary rocks of the Swabian-Franconian Alb as well as the underlying Variscan basement, consisting mostly of metagranites, paragneisses, and amphibolites (e.g., Graup, 1978; Hüttner & Schmidt-Kaler, 1999; Von Engelhardt & Graup, 1984). Stöffler et al. (2013) distinguished structurally the inner crater, the inner wall (which probably corresponds to the rim of the primary inner crater, see Wünnemann et al., 2005), and the megablock zone between the inner and outer crater rim as well as the structural outer crater rim. Generally, two different ejecta masses are distinguished: the ballistically ejected *Bunte Trümmermassen* and the overlying suevite (e.g., Stöffler et al., 2013 and references therein).

The *Bunte Trümmermassen* contain melt-free polymict impact breccia, so-called *Bunte Breccia* and allochthonous rotated rocks, which, if over 25 m in size, are referred to as megablocks that were displaced and fragmented during crater formation (e.g., Hüttner & Schmidt-Kaler, 1999; Pohl et al., 1977; Stöffler et al., 2013; Sturm et al., 2015). The Bunte Breccia is consisting of rock and mineral fragments that are derived predominantly from the overlying sedimentary cover, whereas components from the basement occur in low amounts (a few volume %, Von Engelhardt & Graup, 1984; <0.15 wt% Hörz et al., 1983). The shock conditions indicated by the sedimentary components of the Bunte Breccia are generally low, whereas the few basement components can show shock effects >10 GPa (Hörz et al., 1983; Von Engelhardt & Graup, 1984).

Megablocks that are derived from the basement comprise less than 10% of the area covered by all megablocks (Sturm et al., 2015). These so-called crystalline megablocks mostly show relatively few shock effects indicating low shock conditions (e.g., kink bands in biotite, Von Engelhardt & Graup, 1984). However, brecciated gneisses that occur associated with the crystalline megablocks can show evidence of various shock conditions up to a few tens of GPa (e.g., Abadian, 1972; Hüttner & Schmidt-Kaler, 1999; Stöffler et al., 2013; Von Engelhardt, 1990; Von Engelhardt & Graup, 1984). These so-called polymict crystalline breccias can occur within the crystalline megablocks, as irregular bodies overlying the Bunte Breccia (Abadian, 1972; Arp et al., 2019), and as veins within the basement, as shown by the FBN1973 research drill core north of Nördlingen (Stöffler et al., 1977). In the FBN1973 research drill cores, veins of brecciated cataclastic material occur in up to 1187 m depth (Stähle & Otteman, 1977; Stöffler et al., 1977). These breccias contain fragments of basement rocks and pre-impact veins containing calcite and fluorite (Stähle & Otteman, 1977) as well as fragments of the sedimentary cover sequence, that above 890 m also include limestones (Stöffler et al., 1977).

Shock effects in various minerals reflecting transformation at high shock pressures have extensively been studied in Ries impactites (e.g., coesite/stishovite: Stähle et al., 2008; diamond: Hough et al., 1995; zircon/reidite: Erickson et al., 2017; Stöffler et al., 2013 and references therein). Studies on shocked calcite, however, are generally scarce and restricted to suevites (e.g., Graup, 1999; Osinski, 2003) and limestone megablocks (Skála, 2002).

Here, we analyze calcite-bearing metagranite cataclasites within the gneisses of the crystalline megablocks at Maihingen, which are part of the *Bunte Trümmermassen* (e.g., Abadian, 1972; Graup, 1978; Von Engelhardt, 1997) and from the 1973 research drill cores (e.g., Stähle & Otteman, 1977; Figures 1 and 2).

METHODS

Calcite-bearing metagranite cataclasites were sampled at outcrops of Langenmühle II (48°56′2.04″ N; 10°29′12.04″ E) close to the village of Maihingen (Figure 1). Samples from the 1973 research drilling (Figure 1) cored at depths of 975.4 and 977.65 m were selected at the *Zentrum für Rieskrater- und Impaktforschung Nördlingen* (ZERIN) of the *RiesKraterMuseum Nördlingen*.

All microscopic analyses were conducted on polished thin sections with approximately 25 µm thickness. The microfabrics were analyzed by polarized light microscopy and scanning electron microscopy (SEM), including energy dispersive spectroscopy (EDS) and electron backscattered diffraction (EBSD). For electron microprobe (EMP) measurements, the samples were carbon coated. For EBSD analysis, the samples were further mechano-chemically
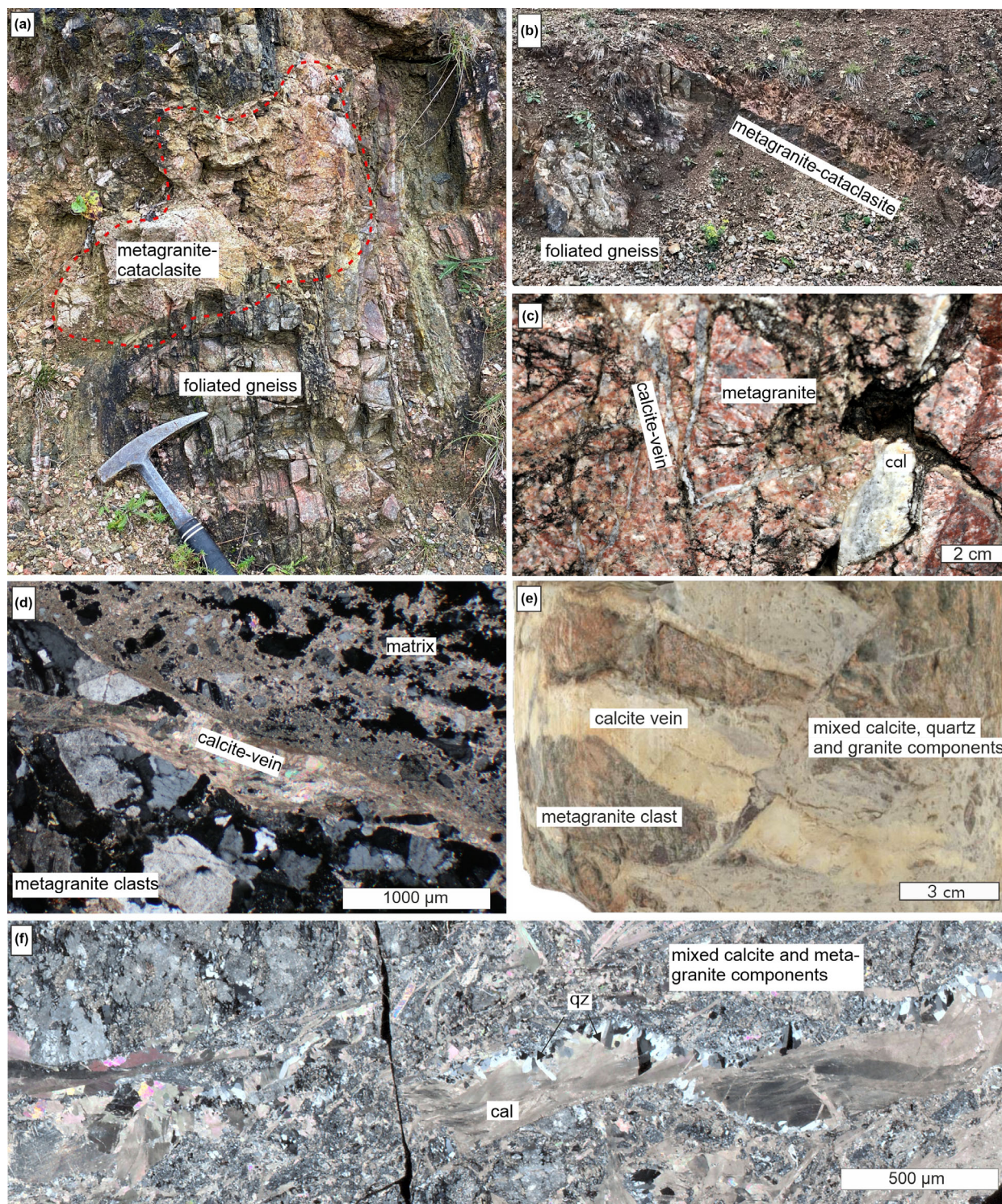
FIGURE 2. Calcite-bearing metagranite cataclasites at outcrop Langenmühle II, near Maihingen (a–d) and in drill core FBN1973 at about 970 m depth (e, f). (a) Lens of calcite-bearing metagranite cataclasites within foliated gneisses. (b) Vein of calcite-bearing metagranite cataclasite within foliated gneisses. (c) Close up of calcite-bearing metagranite cataclasites. (d) Polarized light micrograph showing twinned calcite in veins crosscutting a metagranite calcite clast in the matrix (crossed polarizers). (e) Light yellowish carbonate veins, crosscutting grayish matrix comprised of fine-grained carbonate and metagranite fragments surrounding larger metagranite clasts. (f) Polarized light micrograph (crossed polarizers) shows twinned calcite (cal) and quartz (qz) in veins hosted by the calcite-bearing metagranite cataclasite. (Color figure can be viewed at wileyonlinelibrary.com)

polished using a highly alkaline colloidal silicon suspension. SEM observations were performed using a field emission Hitachi SU5000 microscope, equipped with a NordlysNano high-sensitivity EBSD detector (Oxford instruments) and an EDS detector (Oxford instruments). For acquiring the EDS and EBSD signals the Aztec analysis software (Oxford technology) was used. The SEM was operated at accelerating voltages of 20 kV and a working distance of 10 mm (for EDS measurements) and 20–25 mm (for EBSD measurements). The step size for automatic EBSD mapping using a sample holder pre-tilted at 70° with respect to the horizontal was in the range of 0.5–2 μm, dependent on the EBSD pattern quality and required resolution. For EBSD data acquisition, 43 (hkl) planes of highest intensity of the calcite structure ($a = 4.99$ Å, $c = 17.064$ Å, Laue group 7 (-3 m)) were used. Band detection was set to band edges and eight bands. Measurements with a mean angular deviation $>1°$ from the theoretical pattern have not been considered. The EBSD data were processed using the Channel5 software (Oxford Instruments). Single pixels that are different from the surrounding pixels sharing a common but different orientation and non-indexed points were automatically replaced with the orientation extrapolated from six surrounding pixels. Misorientations are analyzed by characterizing the lowest angle that enables to rotate one orientation into another, that is, by the misorientation angle and the misorientation axis (Wheeler et al., 2001). Twin boundaries are defined by the crystallographically controlled misorientation angle and misorientation axis with a maximum deviation angle of 5°. Grains are detected by a misorientation angle threshold of 10°. These settings were controlled by comparing the resulting orientation maps with the band contrast map, to avoid artifacts. All pole figures are stereographic projections of the lower hemisphere.

The chemical composition of calcite was measured using a Cameca SX-100 electron microprobe at the Department for Earth and Environmental Sciences, LMU Munich. To avoid damaging of the beam-sensitive calcite, the following conditions were applied: 15 kV accelerating voltage, 10 nA sample current, and a 5 μm defocused beam. The calibration was performed using the following silicate and oxide standards: albite (Na), quartz (Si), orthoclase (K, Al), hematite (Fe), periclase (Mg), dolomite (Ca), and bustamite (Mn).

For transmission electron microscopy (TEM) a thin foil was cut across a twinned calcite by focused ion beam (FIB) preparation using a FEI Quanta 3D FEG FIB-SEM instrument. The ablation of material was performed using a Gallium ion beam, while the sample area was imaged by secondary electron (SE) and backscattered electron (BSE) techniques. The Ga ion gun was operated at 30 kV with a beam current between 30 and 0.1 nA for sample preparation. A deposited Pt stripe was used to protect the surface. To remove amorphous layers on the FIB cut, the foils were cleaned at 5 kV using 48 pA beam current. Conventional bright-field TEM images, selected area electron diffraction (SAED) patterns as well as high-angle annular dark-field (HAADF) images were taken with a FEI Technai G^2 FEG TEM, operating at 200 keV and using a double tilt holder. HAADF images were recorded at short (100 mm) and long (2 m) camera lengths, to obtain almost pure Z contrast and diffraction contrast information, respectively.

RESULTS

Sample Description

Basement rocks crop out over about 300 m between the Klosterberg (48°55′48.6″ N 10°29′25.4″ E) and Langenmühle (48°56′06.5″ N 10°29′02.7″ E), representing crystalline megablocks (e.g., Abadian, 1972; Graup, 1978; Sturm et al., 2015; Von Engelhardt, 1997; Figure 1). They comprise metadiorites, amphibolites, metagranites, and garnet-bearing gneisses. At the small former quarry Langenmühle II (48°56′02.0″ N 10°29′12.4″ E), calcite-bearing metagranite cataclasites occur as dm-sized irregular lenses (Figure 2a) and dm-wide veins (Figure 2b) within the foliated gneisses. The cataclasites comprise coarser metagranite clasts of a few cm in diameter, twinned calcite in veins of a few mm to cm in width, and a matrix with mixed metagranite and calcite clasts varying in diameter from several μm to cm (Figure 2c,d).

Similar cataclasites that comprise coarse twinned calcite in veins and a grayish matrix of mixed calcite and metagranite clasts surrounding coarser metagranite clasts (Figure 2e,f) are also present in the cores from the 1973 research drilling at depths of 975 m and 977 m. The coarse twinned calcite in veins is commonly associated with hypidiomorphic quartz (Figure 2f) and subordinate fluorite.

In the rocks from both localities, next to the twinned calcite clasts (cal1) in veins mixed with metagranite components (mc) (Figure 3), also untwinned calcite occurs in matrix and veins (cal2, Figure 3c–f) but always adjacent to twinned calcite. Calcite grain diameters vary from several hundred μm to only few μm within fine-grained aggregates (Figure 3a). Calcite-rich veins can crosscut metagranite components (Figure 3a,b,d–f) as well as calcite components (Figure 3c,d). Calcite can occur as elongate laths in the matrix surrounding clasts of metagranite (white arrow in Figure 3b) as well as in veins (Figure 3f). Inclusion-poor quartz growth rims can be present at the contact of metagranite clasts to the calcite-rich matrix (red arrow in Figure 3b).
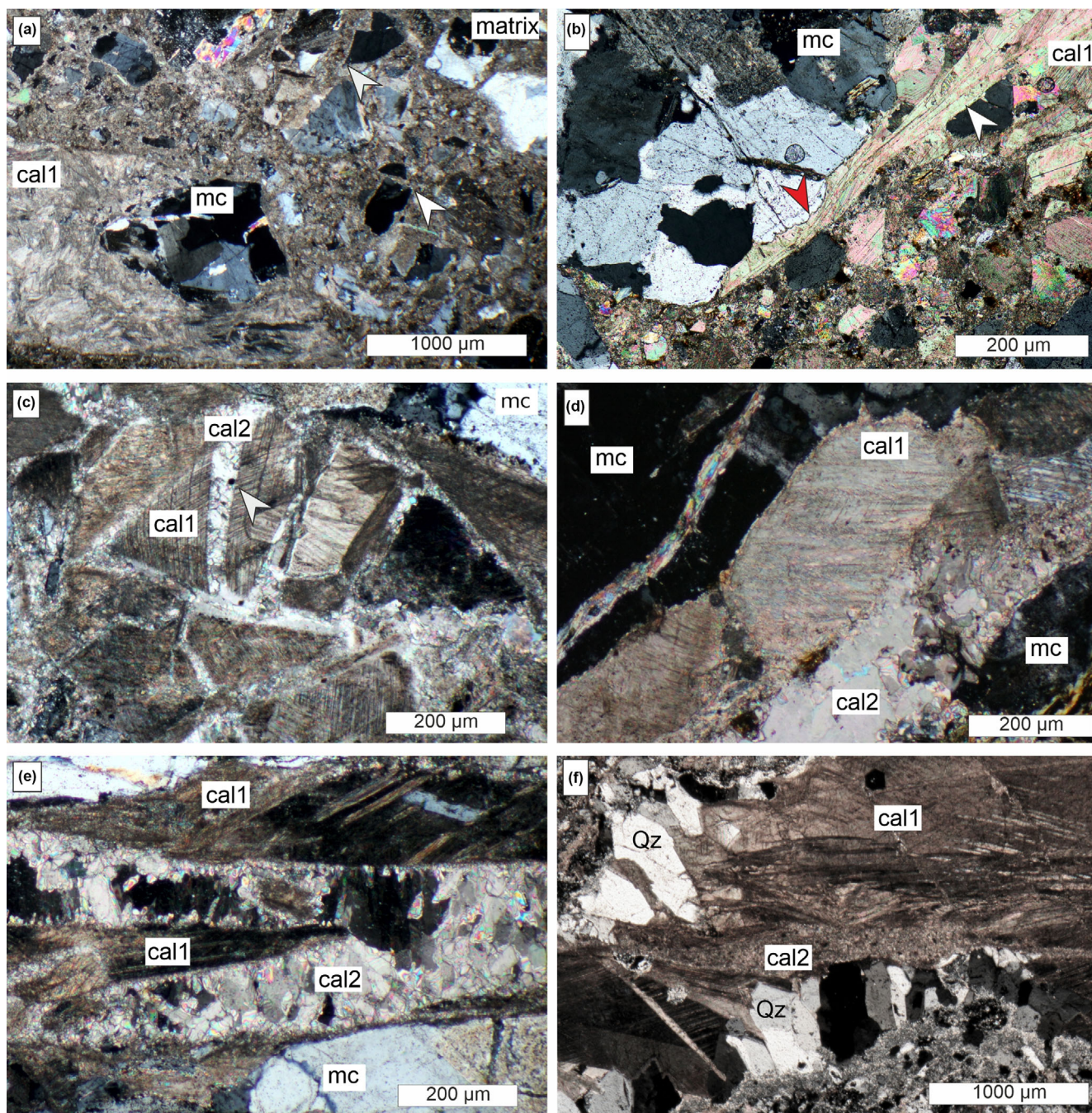
FIGURE 3. Polarized light micrographs (crossed polarizers) showing calcite microstructures in samples from Langenmühle II, Maihingen (a–e), and within drill core sample (f). (a) Fine-grained calcite and twinned coarse-grained calcite components (cal1) together with metagranite components (mc) form the matrix and components of the cataclasites. Fine-scaled veins crosscut minerals from the metagranite (white arrows). (b) Metagranite component (mc) surrounded by a twinned, elongate calcite grain (cal1). Quartz grain of metagranite component shows inclusion-free growth rim (red arrow). (c) Untwinned calcite vein (cal2) crosscutting twinned calcite (cal1) (white arrow). (d, e) Untwinned calcite (cal2) and twinned calcite (cal1) in vein crosscutting metagranitic gneiss components (mc). (f) Elongate twinned calcite (cal1) in vein with hypidiomorphic quartz crystals and fine-grained, untwinned calcite (cal2). (Color figure can be viewed at wileyonlinelibrary.com)

In veins, the untwinned calcite (cal2) can be elongate with a palisade shape and the long axis perpendicular to the vein wall (Figure 4a). Untwinned calcites (cal2) that occur between twinned crystals (cal1) typically have an isometric grain shape and are a few µm in diameter (Figure 4b,c). Untwinned growth rims
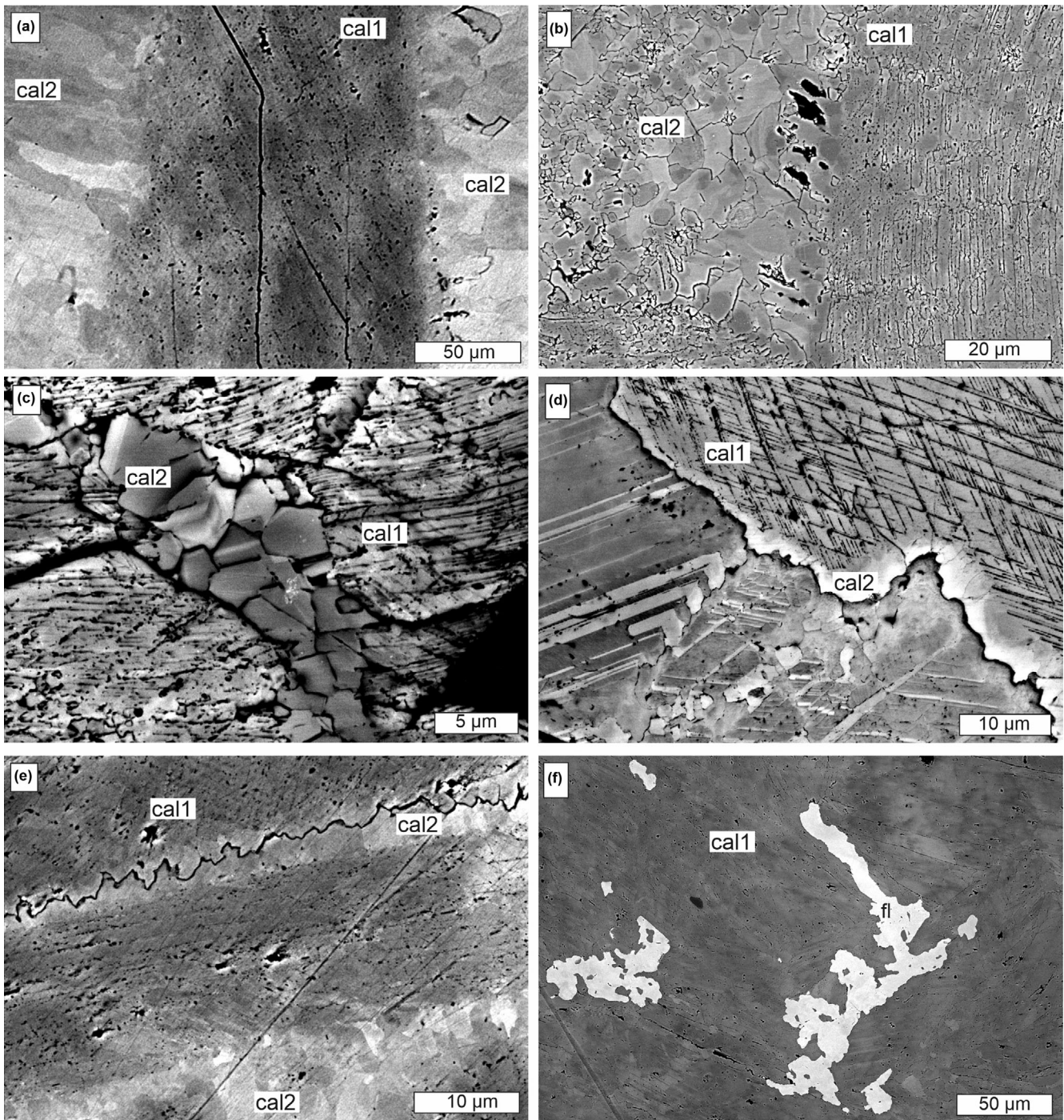
FIGURE 4. Calcite BSE images (a-e) samples at Langenmühle II and (f) drill core sample. (a) Palisade-shaped untwinned calcite (cal2) in contact with twinned calcite (cal1) in the vein. (b, c) New isometric, untwinned grains (cal2) within twinned calcite grain (cal1). (d, e) Untwinned rim (cal2) surrounding twinned calcite (cal1) grains, which display sutured grain boundaries. (f) Fluorite (fl) within vein of twinned calcite (cal1).

(cal2) around twinned grains (cal1) lead to sutured grain boundaries (Figure 4d,e). In the calcite veins of the drill core sample, fluorite is locally present (Figure 4f).

The composition of the twinned calcite (cal1) in the cataclasites of both localities is almost pure $CaCO_3$ with up to 1 wt% MnO, below 0.2 wt% MgO, and below 0.15 wt% FeO (total Fe content, no differentiation between Fe^{2+} and

Table 1. Electron microprobe measurements.

JB2	CaO (%)	D.L. Ca (ppm)	MgO (%)	D.L. Mg (ppm)	MnO (%)	D.L. Mn (ppm)	FeO (%)	D.L. Fe (ppm)	CO2 (%)	Total (%)
Cal1	54.29	670	0.21	358	0.53	1088	0.02	1055	44.96	100.00
Cal1	53.79	633	0.03	417	0.79	966	0.14	1069	45.24	100.00
Cal1	53.84	636	0.17	360	0.55	1013	0.06	1100	45.38	100.00
Cal1	53.82	649	0.19	394	0.73	1157	n.d.		45.26	100.00
Cal1	54.15	591	0.10	423	0.72	1021	0.04	1094	44.99	100.00
Cal1	54.24	573	0.12	414	0.69	1028	0.04	1118	44.91	100.00
Cal1	55.05	572	0.03	364	0.15	1012	n.d.		44.77	100.00
Cal1	53.65	617	0.33	419	0.40	1062	0.07	1121	45.54	100.00
Cal1	53.87	626	0.08	369	0.43	905	0.04	1039	45.59	100.00
Cal1	54.28	597	0.07	366	0.34	994	n.d.		45.31	100.00
Cal1	54.02	615	0.06	401	0.30	1056	n.d.		45.62	100.00
Cal2	52.34	630	0.22	432	0.60	1071	2.36	1117	44.47	100.00
Cal2	53.41	584	0.19	387	0.37	947	1.51	1053	44.51	100.00
Cal2	52.09	645	0.26	388	0.56	1047	2.42	1163	44.67	100.00
Cal2	53.67	580	0.24	416	0.36	1031	2.77	1196	42.97	100.00
Cal2	52.30	637	0.24	373	0.46	1002	2.13	1128	44.86	100.00

Note: D.L. refers to the detection limit. Electron microprobe measurements on twinned calcite grains (Cal1) and untwinned calcite in growth rims around twinned calcite (Cal2) in sample of polymict crystalline breccia from Langenmühle (sample JB2).

Abbreviation: n.d., not detected.

Fe^{3+}) as indicated by EDS and EMP measurements (Table 1). The composition of the untwinned calcites (cal2) in the Langenmühle samples show higher Fe contents with up to about 3 wt% FeO and a slight enrichment in MgO, as indicated by EDS and EMP measurements (Table 1) as well as evident by the lighter gray in BSE images (Figure 4a–e). In contrast, the untwinned calcites (cal2) in the drill core samples are also pure $CaCO_3$, as the twinned calcites (cal1) from both localities.

The observation of twinned calcite components in the cataclasites from both localities (cal1, Figures 2d,f and 3) is inconsistent with late post-shock precipitation from a hydrothermal fluid. The impact structure was not subject to major tectonic deformation after the impact event except for some subsidence (Arp et al., 2021). Calcite veins with locally occurring fluorite are known to occur in metagranites and gneisses of the Variscan basement that can be correlated with the basement rocks in the Ries impact structure (e.g., Graup, 1977, 1978; Hüttner, 1977; Stähle & Otteman, 1977). Thus, the twinned calcite components (cal1) as well as the metagranite components are interpreted to originate from the Variscan basement, that is, they belong to the crystalline megablock. Nevertheless, it cannot be excluded that some calcite may also originate from the sedimentary cover. Limestone clasts from the sedimentary cover within crystalline breccias are described for the 1973 research drill core (e.g., Stöffler et al., 1977).

The metagranite components in both samples include altered feldspar, kinked biotite, chlorite, and Fe-oxides (Figures 2e and 3b). No planar deformation features were observed in quartz, which indicates low shock conditions of <7 GPa (shock stage F-S2 according to Stöffler et al., 2018).

Calcite Twins

All twin systems known as mechanical twins for calcite, that is, *e*-, *f*-, and *r*-twins, were identified by EBSD analysis in the twinned calcite (cal1) of the cataclasites (Figures 5 and 6). Generally, *e*-, *f*-, and *r*-twins are coherent twins, that is, they have a common twin and composition plane, where the twin is characterized by a rotation with respect to the host of 180° about the pole of an $e\{01\bar{1}8\}$, $f\{01\bar{1}2\}$, and $r\{10\bar{1}4\}$ rhombohedral plane, respectively (e.g., Barber & Wenk, 1979; Schuster et al., 2020). This twinning results in a specific misorientation between the twin and the host, which can be analyzed by EBSD.

The most commonly observed calcite twins in our samples are *e*-twins, which are in the EBSD data characterized by a misorientation angle of 78°, and a misorientation axis parallel to $<20\bar{2}1>$, which is the pole to an $\{10\bar{1}4\}$ plane. Furthermore, *r*-twins (Figure 5) occur with twin boundaries parallel to the $\{10\bar{1}4\}$ rhombohedra, identified by a misorientation angle of 100° and a misorientation axis parallel to $<0\bar{4}41>$ in the EBSD data. Note that the *r*-twin lamellae can cut through the host and *e*-twin lamellae without deflection (Figure 5a,b), because all three domains have a common $\{10\bar{1}4\}$ plane. The *e*-twins can themselves be twinned containing secondary *e*- as well as *r*-twins that terminate
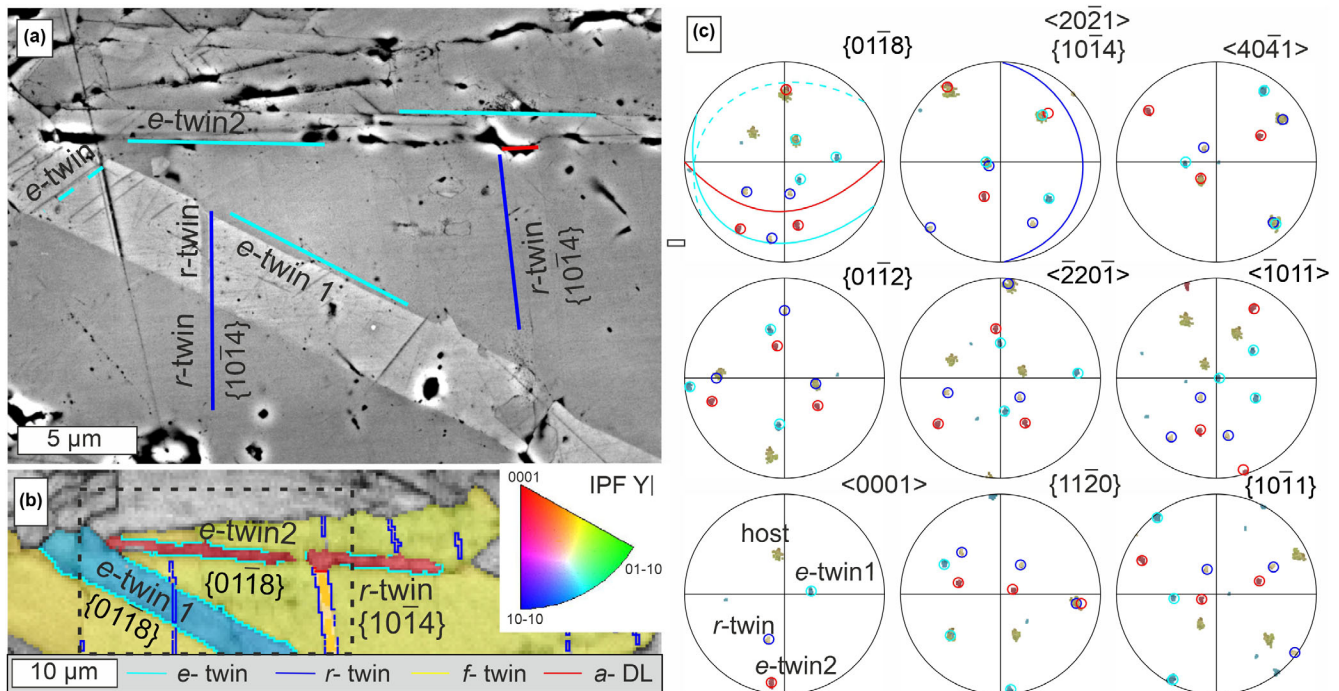
FIGURE 5. Twinned calcite within a vein, FBN1973 drill core sample. (a) BSE image and (b) EBSD map (color coding according to inverse pole figure of the vertical direction within the image plane, IPF Y) showing twinned calcite crystal with e-twin and r-twin lamellae. Note that e-twin lamella 1 (blue/turquoise) is containing secondary fine-lamellar e-twins only observable in the BSE image in (a), area indicated by black-rimmed rectangle. (c) Corresponding pole figures of host grain (yellow), e-twin (turquoise lines), r-twin (blue lines). Note that the r-twin and e-twin 2 are showing an a-type crystallographic relationship (red line, a-DL). (Color figure can be viewed at wileyonlinelibrary.com)

at the boundary to the primary e-twin (Figure 5a,b). When e- and r-twins that have a common a-plane (Figure 5c) crosscut each other, a specific boundary between these two twin domains is characterized by a misorientation angle of about $35 \pm 10°$ and a misorientation axis parallel to $<11\bar{2}0>$ (red line in Figure 5b). Such a crystallographic relationship has been observed between so-called a-type lamellae and their host calcite grains formed at high strain (>100) deformation experiments at room temperature and 1–4 GPa confining pressure by Schuster et al. (2020).

In addition, f-twins can occur in the EBSD data characterized by twin planes parallel to $\{01\bar{1}2\}$ rhombohedral planes, a misorientation angle of 78°, and a misorientation axis parallel to $<\bar{2}20\bar{1}>$ (Figure 6). The f-twins can themselves contain secondary r-twins as identified by combined TEM (Figures 6a and 7b) and EBSD (Figure 6c,d) analysis. The r-twinned f-twins result in an a-type domain characterized by a misorientation angle of $35 \pm 10°$ and a misorientation axis parallel to $<11\bar{2}0>$ relative to the host calcite (Figure 7c,d), analogous to the misorientation between r- and e-twins in Figure 5 and the a-type domains observed from the high strain experiments of Schuster et al. (2020). The secondary r-twin boundaries within the f-twins appear in

the EBSD map (Figure 6d) as irregular boundaries. Yet, TEM reveals that the secondary r-twins in the f-twins result in serrated boundaries to the host, which are partly parallel to the primary f-twin and partly parallel to the secondary r-twin (Figure 7b).

In TEM (Figure 7) and BSE images (Figure 8), the thickness of the twin lamellae is found to be typically on the order of tens to hundreds of nm. Rarely, e-twins can show a width of up to 5 μm in BSE images and EBSD maps (Figure 5a,b). Generally, no evidence of twin boundary migration, for example by sutured twin boundaries, is present. At the intersection between different twin lamellae voids, so-called Rose channels (Barber & Wenk, 1979; Langenhorst et al., 2003) can be observed in TEM (black arrows in Figure 7f) and BSE images, where e- and f-twins (white arrows in Figure 8a), or e- and r-twins (white arrows in Figure 8b) crosscut each other. Primary e-twins can contain secondary e-twins (Figures 5a and 8d), secondary f-twins (Figure 8e), and secondary r-twins (Figure 5a). Primary f-twins can contain secondary r-twins (Figures 6d and 7b, e). Three different e-twin lamellae can occur in one grain (Figure 8b). In TEM, a high dislocation density (on the order of 10^{14} m^{-2}) is revealed associated with
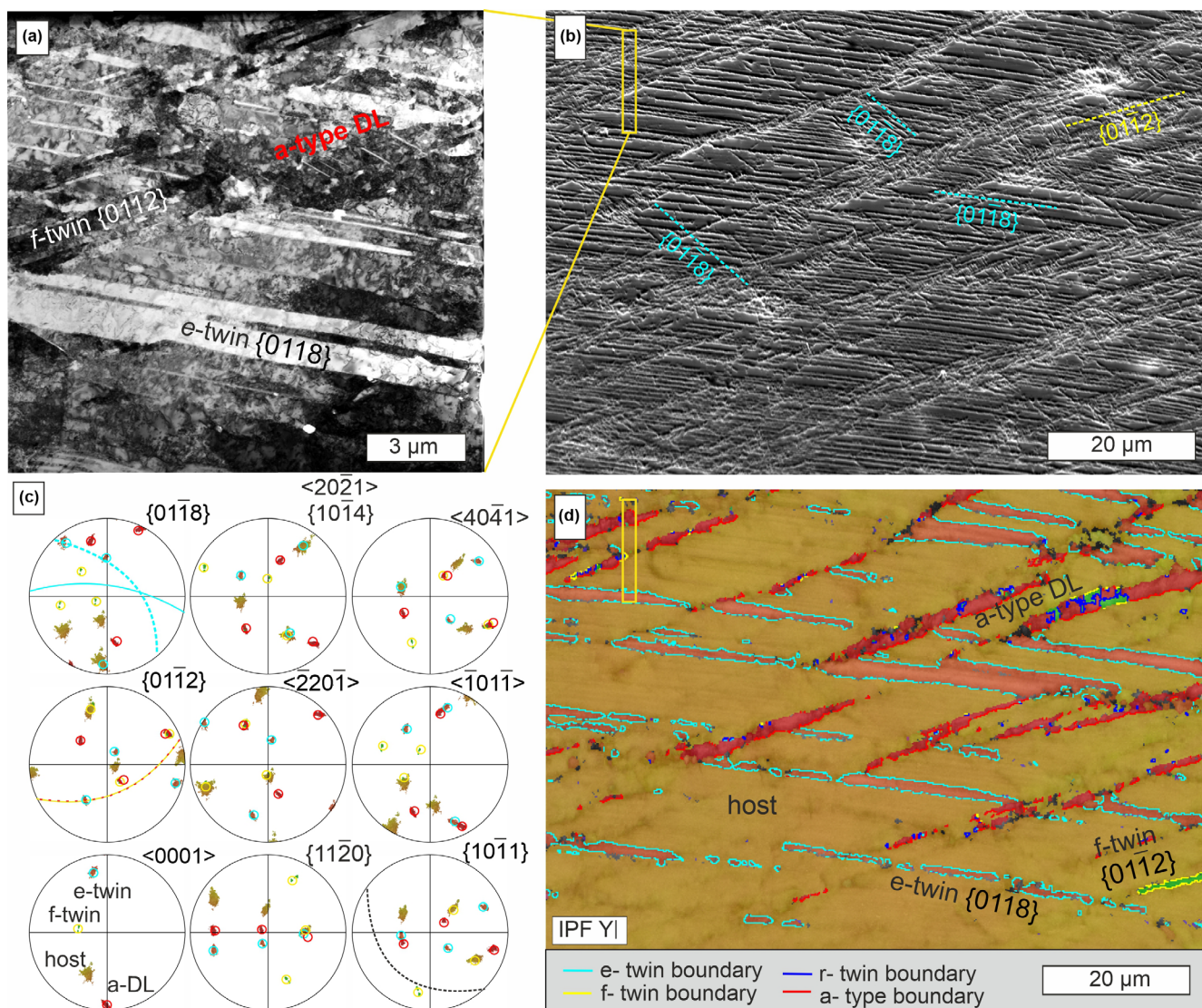
FIGURE 6. Twinned calcite within a vein (cal1), sample Jb2-a (Langenmühle II). (a) TEM-diffraction image, location shown in (b). (b) SE image showing high density of fine twin lamellae. (c) Pole figures of host grain (orange), *e*-twin (dark orange), *f*-twin (green), and *a*-type lamellae (red) projected in the plane of the EBSD map (d). (d) EBSD map (IPF Y color coding) with twin boundaries indicating *e*-, *f*-, and *r*-twins, as well as the *a*-type lamellae. Note that the *a*-type lamellae are related to the misorientation of the host and *r*-twinned *f*-twins. (Color figure can be viewed at wileyonlinelibrary.com)

the twins and at the intersection of different twin lamellae (white arrows in Figure 7a–c). Note especially the effect of the *r*-twins on the boundary of the primary *f*-type twins leading to *a*-type domains (red arrows in Figure 7b–d, compare also Figure 6c,d). The interaction between the different twins can also lead to slightly rotated crystal domains with misorientation angles $<20°$ (red arrows in Figure 8c,e,f). Generally, the twin density is exceptionally high with $>1/\mu m$ (Figures 7 and 8).

The twin density can vary with a tendency of an increased density at the rim of veins to the matrix

(Figure 9). Directly at the contact of a calcite vein to the matrix of the cataclasite, a fine-grained $CaCO_3$ aggregate occurs that could not be indexed by EBSD (due to the small grain size and/or due to a high defect density) and which is followed by a fine-grained aggregate of untwinned calcite grains toward the contact of the twinned calcite in the vein with decreasing twin density towards the vein center. The untwinned calcite (cal2) shows a broad range in orientations but a maximum corresponding to that of the twinned coarse calcite (Figure 9c,d). The relative misorientation angle within
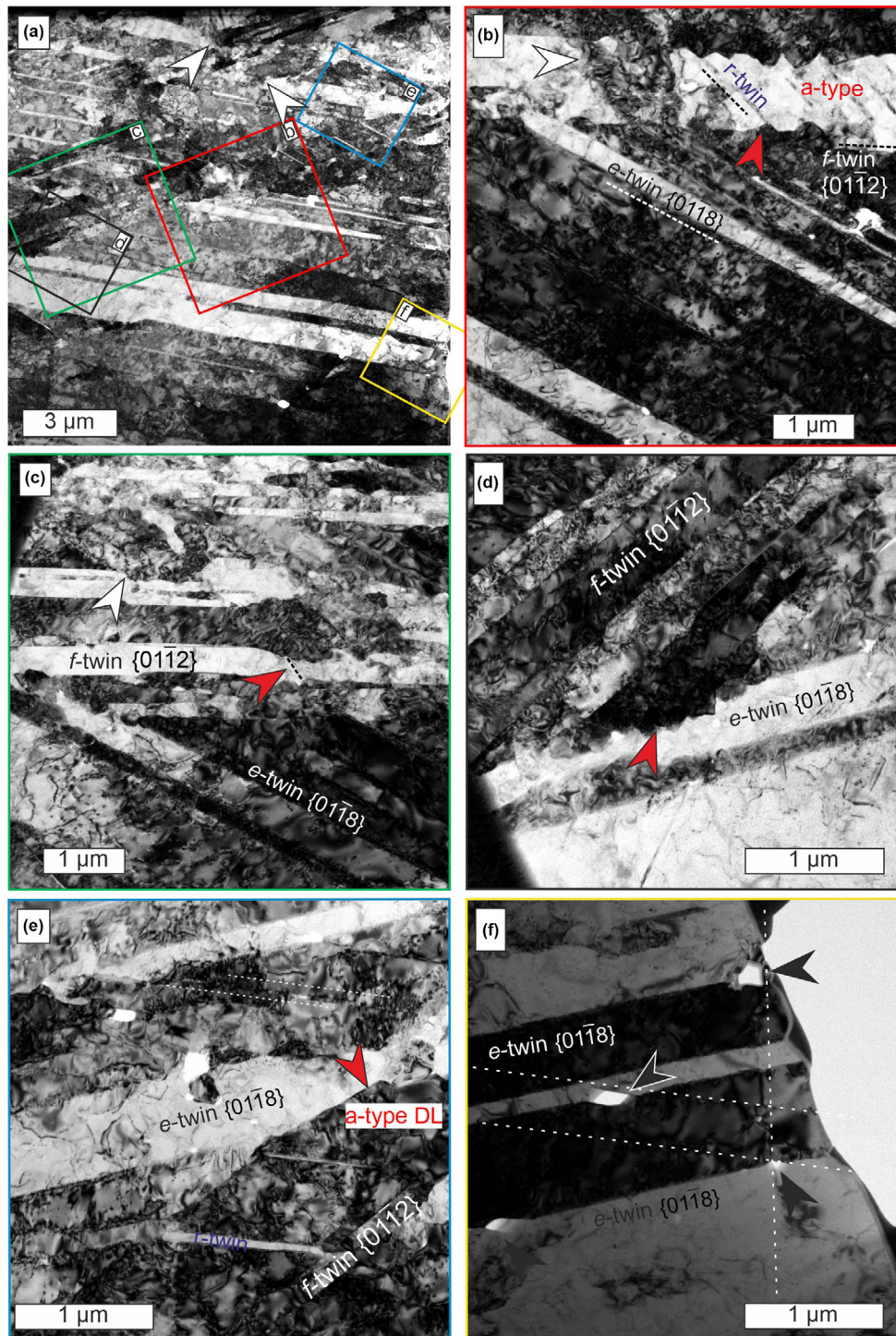
FIGURE 7. Bright-field TEM images from sample area shown in Figure 6b,d. (a) Locations of images (b–f) are indicated by colored rectangles. Note the thin *r*-twin lamellae in the *a*-type domain, compare Figure 6d. The white arrows point to high dislocation densities at the intersection of twins. The red arrows show the serrated boundaries of *a*-type domain related to *r*-twins in an *f*-twin lamellae. Black arrows in (f) mark voids at the intersection between different twin lamellae. (Color figure can be viewed at wileyonlinelibrary.com)

these grains, indicated by the angular deviation from the average grain orientation, is generally below a few degrees (Figure 9a).

Elongate twinned calcite grains (cal1) in veins have commonly been observed (Figure 3b,f) that have a *c*-axis perpendicular to the long axis of the host grain
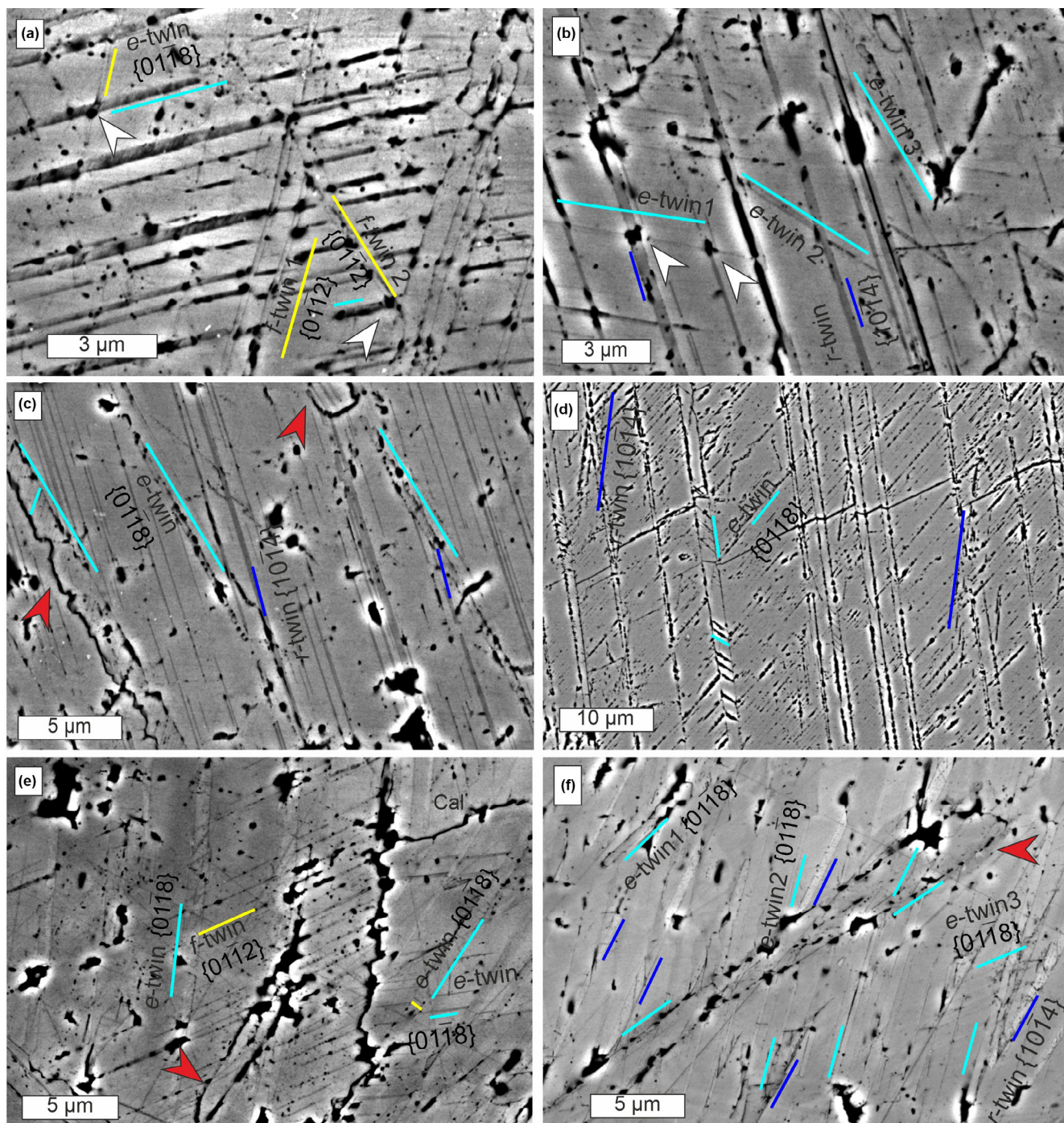
FIGURE 8. BSE images showing twinned calcite from sample JB2b, Langenmühle II (a–d) and the FBN73 drill core sample FBN73-21_3 (e, f, compare Figure 10a). White arrows mark so-called Rose channels. Red arrows point to slightly rotated crystal domains without specific misorientation (<20°). (a) Crosscutting e- and f-twin lamellae. (b) Crosscutting r- and e-twin lamellae. Three different e-twins occur. (c, d) Crosscutting e- and r-twin lamellae. Note that e-twin lamellae can contain themselves e-twin lamellae. (e) e- and f-twin lamellae. Note that e-twin lamellae can contain themselves f-twin lamellae. (f) Crosscutting r- and e-twin lamellae, which can end at the intersection. (Color figure can be viewed at wileyonlinelibrary.com)

(Figure 10). In larger aggregates of calcite with high twin densities (cal1, compare Figure 10a and corresponding BSE images in Figure 8e,f), also grain orientations without specific crystallographic relationships and misorientations typically below 20° from the host orientation are observed that can result in low angle grain
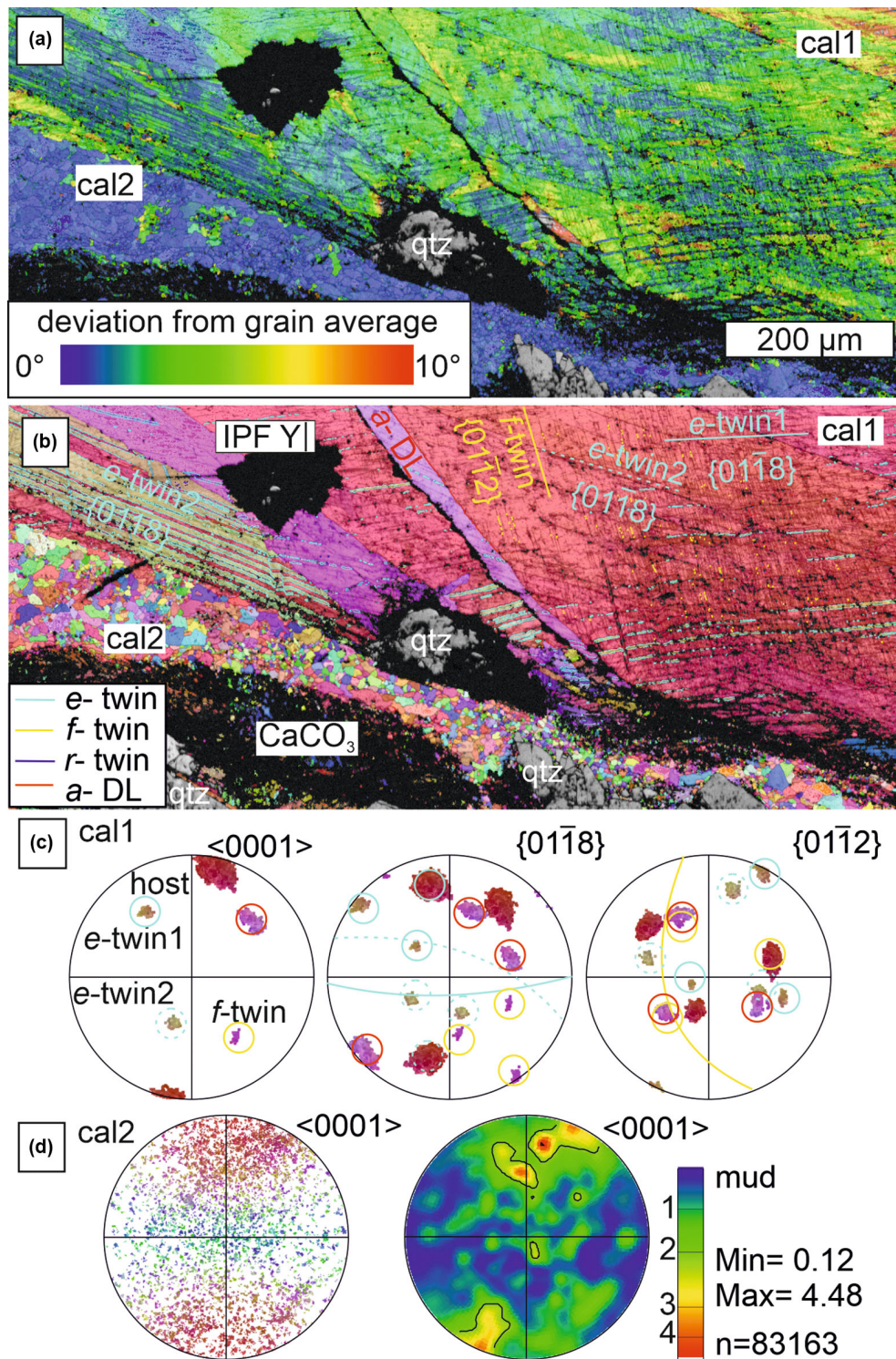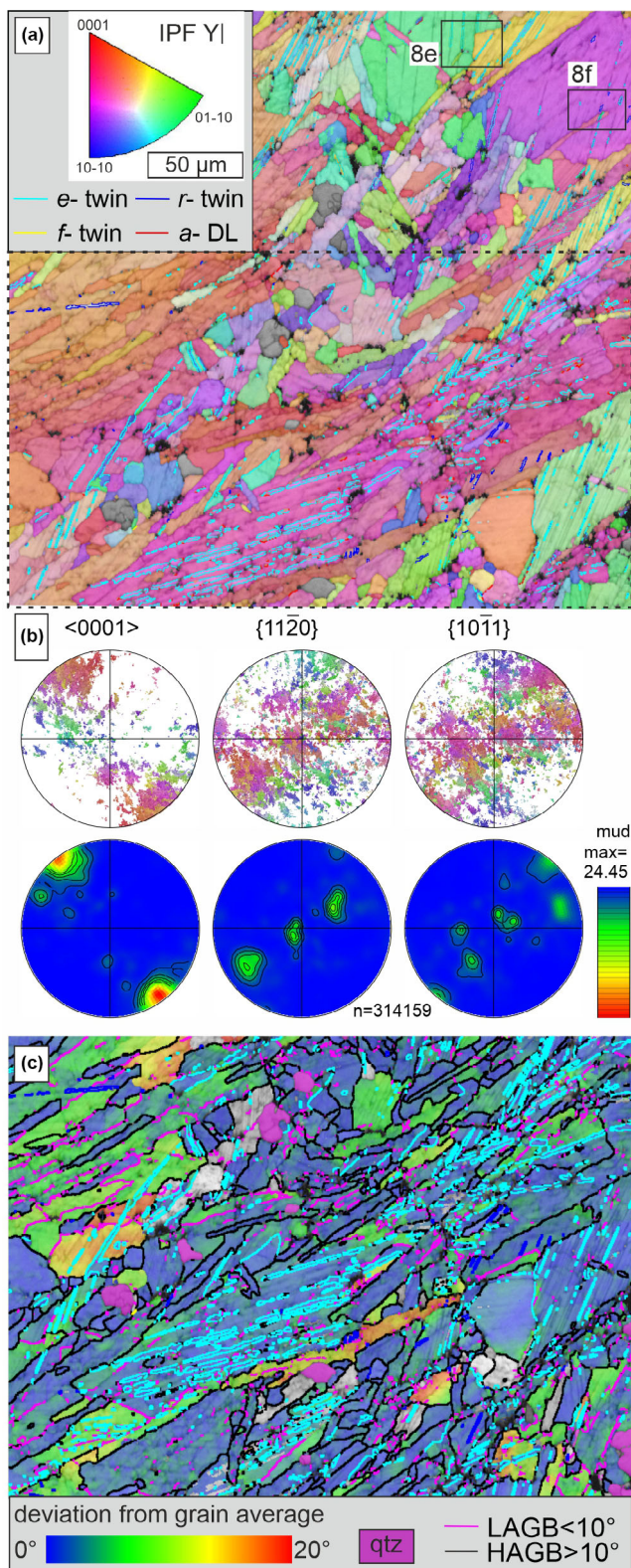
FIGURE 9. EBSD data of FBN73 drill core sample (FBN73-21_1). (a) Grain Reference Orientation Deviation map (GROD, angular deviation from the average grain orientation) and (b) EBSD map (IPF Y) of twinned calcite in a vein (cal1), drill core sample. Fine-grained untwinned calcite (cal2) aggregates and a zone of not-indexed $CaCO_3$ at the contact to quartz crystals at the boundary to the vein. Note the increasing twin density at the contact to the fine-grained calcite. (c) Crystallographic orientation of the coarse twinned calcite and (d) of the fine-grained calcite with density plot. Note the almost random orientation of the fine-grained calcite aggregate but weak maximum close to the orientation of the coarse adjacent grain. (Color figure can be viewed at wileyonlinelibrary.com)

FIGURE 10. EBSD data of vein in drill core sample FBN73-21_3. (a) EBSD map (IPF Y) of twinned calcite in a vein (cal1), drill core sample (compare BSE images Figure 8e,f) and (b) corresponding pole figures of c-axes, $\{11\bar{2}0\}$ prism and $\{10\bar{1}1\}$ rhombohedral planes and density plots. Note the shape and crystallographic preferred orientation with the c-axes perpendicular to the long axes of grains. (c) GROD map (angular deviation from the average grain orientation) of area indicated by rectangle in (a) with low ($<10°$) and high ($>10°$) angle grain boundaries indicated by pink, respectively, black lines in addition to twin boundaries. Quartz grains are marked as pink phase. (Color figure can be viewed at wileyonlinelibrary.com)

be up to 20°, especially in calcite grains that are in direct contact with isolated quartz inclusions (Figure 10c).

DISCUSSION

Comparison with Previous Studies on Calcite Twinning

The fine-lamellar twins with widths of <100 nm occurring in densities of $>1/\mu m$ (Figures 7 and 8) compare well to the early deformation experiments of Barber and Wenk (1979) as well as to those from shock experiments (Kenkmann et al., 2018; Kurosawa et al., 2022; Langenhorst et al., 2003). Langenhorst et al. (2003) observed similarly fine-lamellar twins, as well as a second generation of twins, that is, multiple twinning. However, in the shock experiments on single crystals of Langenhorst et al. (2003), no e-twins were observed, which is possibly related to unsuitable orientations to the principal stress directions, that is, an insufficiently high resolved shear stress on the twin plane. Here, we observe e-, f-, and r-twins in single calcite crystals, which requires that the critical resolved shear stress was reached for all twin systems. We observe multiple twinning, where primary e-twins can contain secondary e-twins (Figures 5a and 8d), secondary f-twins (Figure 8e), and secondary r-twins (Figure 5a) and primary f-twins can contain secondary r-twins (Figures 6d and 7b,e).

The interaction between different twin domains commonly leads to a specific crystallographic relationship characterized by a misorientation angle of $35 \pm 10°$ and a misorientation axis parallel to a pole of an a $\{11\bar{2}0\}$ prism plane (Figures 5 and 6). This a-type relationship has been specified to occur between crosscutting e- and r-twins with a common a-plane in one host crystal (Figure 5) and between the host calcite and secondary r-twins in primary f-twins leading to the a-type domains (Figures 6 and 7b). The a-type relationship and the interaction between e- and r-twins and r- and f-twins has been similarly found in high shear strain deformation experiments at relatively high static pressures (1–4 GPa)

boundaries (yellow lines in Figure 10c). The relative misorientation angle within single grains, indicated by the angular deviation from the average grain orientation, can

by Schuster et al. (2020). The interaction between strongly twinned crystals can also lead to new orientations without specific crystallographic relationships and misorientations typically below 20° from the host orientation (Figures 8c,e,f and 10). The twin-related grain rotation is consistent with the observation of an enhanced high dislocation density, where different twin lamellae crosscut each other (Figure 7). An enhanced dislocation density can be explained by strain accommodation during multiple twinning by dislocation glide, by the increased stresses at the tip of the propagating twin boundaries (Barber & Wenk, 1979) and by strain hardening, given that the twin boundaries act as obstacles to dislocation glide (e.g., Rybacki et al., 2021). However, voids, the so-called Rose channels, can also be present at the twin intersections, as observed in TEM (black arrows in Figure 7f) and BSE images, where e- and f- (white arrows in Figure 8a), or e- and r-twins (white arrows in Figure 8b) crosscut each other. These Rose channels have similarly been observed in shock experiments by Langenhorst et al. (2003) and the deformation experiments by Barber and Wenk (1979). These authors interpreted the voids to result from multiple twinning. Whether voids or dislocations are produced might be controlled by the local orientation of the crystal to the principal stress directions, that is, the Schmid factor for the given twin system. The interaction of the different twin domains further results in serrated boundaries, representing the boundary between primary or secondary twins to the host or crosscutting other twins (red arrows in Figure 7b–e). In TEM, no evidence of recovery, for example, by well-ordered subgrain boundaries, is observed that would indicate effective dislocation climb.

The deformation experiments by Rybacki et al. (2021), which demonstrated that the concurrent activation of twinning, dislocation glide, and fracturing in calcite, that is, twinning-induced plasticity in calcite at low temperatures, are consistent with our observations. Evidence for fracturing of calcite is prerequisite for the cataclasites and indicated by the twinned calcite clasts that are cemented by untwinned calcite (Figures 2 and 3).

In tectonic fault rocks, e-twins are most common, and the width of the twins is found to correlate with temperature (Burkhard, 1993; Ferrill et al., 2004): thin twins (<5 μm) are assumed to form at temperatures <200°C, thick twins (>5 μm width) at temperatures >200°C and at temperatures >250°C dynamic recrystallization of calcite with twin boundary migration occurs. Our observed twin microstructures with typical twin width <1 μm, e-, f-, r-twins and a-type lamellae present in a single grain (Figures 6–8), however, differ markedly from those reported in tectonic fault rocks. Only rarely e-twins can show widths of up to 5 μm in BSE images and EBSD maps (Figure 5a,b).

Overall, the microstructure reflects twinning-induced plasticity in calcite, without evidence of recovery (no well-ordered subgrain boundaries) or twin boundary migration (no sutured twin boundaries). The post-shock temperatures were thus rather low preventing effective thermally activated dislocation climb.

Deformation of Calcite During Cataclasis and Mixing

In accordance with the low post-shock temperatures, the absence of shock effects in quartz indicates that the metagranite with calcite veins experienced low shock pressures, that is, below 7 GPa (see Stöffler et al., 2018).

The critical resolved shear stress for calcite twinning is with several tens of MPa relatively low (e.g., Covey-Crump et al., 2017; Parlangeau et al., 2019). Yet, the activation of different twins and the twin density are known to be strongly dependent on stress, which makes calcite twinning a widely used paleopiezometer (e.g., Lacombe, 2007; Rowe & Rutter, 1990; Rybacki et al., 2013, 2021). Although the experimental setup for the calibration of the twin paleopiezometers largely deviates from the geological conditions during impact cratering, it may still give an estimate on the order of the differential stress during deformation. Applying the calcite twin paleopiezometer by Rybacki et al. (2013), the twin density of fine-lamellar twins of $>1/\mu m$ and widths of <100 nm (Figures 7 and 8) yields differential stresses on the order of 1 GPa. These estimates are comparable to those from twinned calcite in shock experiments by Langenhorst et al. (2003) and Kenkmann et al. (2018). High differential stresses are also consistent with the observation of e- f-, and r-twins together with a-type domains in single calcite crystals, which requires that the critically resolved shear stress was reached for all twin systems. Numerical models predict high differential stresses on the order of several GPa during quasi-instantaneous loading caused by impact even at relatively low shock pressures (Rae et al., 2019, 2021). The relatively low shock pressure suppresses brittle failure on one hand and still allows for sufficient shear stresses and the accumulation of shear strain on the other (Trepmann, 2008).

Burt et al. (2005) reported impact-induced calcite twins from the Meteor Crater, Arizona, and Lindgren et al. (2011) from carbonaceous chondrites both at relatively low shock levels, well consistent with our findings. Kurosawa et al. (2022) observed undulatory extinction of calcite under an optical microscope associated with twins in experimentally shocked samples to >3 GPa. The calcite twins that were generated in experiments by Langenhorst et al. (2003) at shock durations of nanoseconds, that is, strain rates on the order of up to 10^9 s^{-1} formed quasi-instantaneously. In

nature, the shock duration is longer according to the larger diameter of the projectiles, but still on the order of seconds (e.g., Langenhorst et al., 2003; Melosh, 1989). In contrast to these extremely short time scales, also deformation experiments at strain rates of 10^{-4} s^{-1} to 1.7×10^{-2} s^{-1} (with longitudinal/shear strain and not volumetric strain) and at static but relatively high confining pressures (1–4 GPa) from Schuster et al. (2020) and Barber and Wenk (1979) can generate very similar twinning microstructures. All these experiments, though at different time scales, realize high differential stresses at relatively high confining pressures, both on the order of one to few GPa. As high differential stresses are prerequisite for the inferred twinning-induced plasticity, we suggest that the deviatoric component of the shock-related stress is the controlling factor and not the dynamic quasi-instantaneous shock loading to compressive stresses. Yet, a sufficient confining pressure is required to prevent brittle deformation. Thus, in principle, such a twinned calcite microstructure might also be expected in carbonate-rich fault rocks deformed coseismically at high stresses close to hypocentral depths of major earthquakes in the continental crust, which, however, has to our knowledge not been observed so far.

Calcite Crystallization Within the Cataclasites

The veins of twinned calcite crosscutting metagranite clasts and coarse calcite clasts (Figures 2d and 3a–f) as well as the shape of elongate twinned calcite crystals in veins and surrounding metagranite components (Figure 3b,f), indicate that calcite was deformed during cataclasis within the crystalline megablocks. No microstructural evidence for crystallization from a melt (e.g., budding, carbonate globules) or devolatilization and major transport of the components has been identified. That the calcite-bearing metagranites are more strongly affected by cataclasis then the surrounding gneisses (Figure 3a) might be due to the strong contrast of mechanical properties of the metagranite and the calcite veins.

The untwinned calcite (cal2) that shows no evidence of deformation represents a late generation crystallized within the cataclasites, that is, after deformation and formation of the cataclasites. The untwinned calcite growth rims surrounding twinned calcite are enriched in Fe and Mn (Figure 4d,e), indicating grain boundary migration driven by both, chemical gradients and reduction in strain energy, after deformation, that is, static recrystallization and/or precipitation from the pore fluid. The untwinned calcite (cal2) in veins (Figure 3d) that can show palisade structures (Figure 4a) and euhedral crystals in open cavities, is interpreted to have precipitated from a pore fluid subsequent to the impact

event. The chemical variation of calcite growth rims in the Langenmühle samples in contrast to the pure calcite compositions in the FBN1973 drill core samples might indicate the involvement of calcite-rich components of the sedimentary cover and/or the involvement of chemically more variable fluids in the Langenmühle samples.

The increasing density of twins in calcite veins followed by aggregates of untwinned new grains (cal2) and finally in EBSD maps non-indexed $CaCO_3$ (without any chemical difference identified by EDS and EMP) toward the boundary of the vein to the matrix (Figure 9) is interpreted as a strain gradient. The least strained part shows a relatively low twin density (Figure 9a,b). The untwinned grains (cal2) with low internal misorientation (Figure 9a) are interpreted to have grown from strongly deformed calcite driven mostly by the reduction in strain energy, that is, recrystallization, as indicated by the weak crystallographic preferred orientation associated with the orientation of the adjacent coarse grain, which is probably the host crystal (compare Figure 9c,d). An involvement of fluids as discussed above cannot be ruled out, however, here no chemical gradient has been observed. The non-indexed $CaCO_3$ is interpreted to represent a highly strained volume with very fine grain size and/or distorted crystal structure with high defect density.

Overall, the untwinned calcite (cal2) represents a second generation of calcite formed after the impact, as the untwinned grains are strain free (Figure 9a). The occurrence of this young generation of undeformed calcite indicates that the stresses remained low ($<$ a few tens MPa) after their formation.

CONCLUSIONS

Based on the observed microstructures of the calcite-bearing metagranite cataclasites from the Langenmühle II outcrop at the northwestern inner ring and the FBN1973 research drilling (depths of 970 m) north to the city of Nördlingen we conclude the following:

- Twinned calcite (cal1) in the cataclasites is interpreted to originate from pre-shock calcite veins within the rocks of the Variscan basement.
- Primary e-twins can contain secondary e-twins (Figures 5a and 8d), secondary f-twins (Figure 8e), and secondary r-twins (Figure 5a). Primary f-twins can contain secondary r-twins (Figures 6d and 8b,e). Three different e-twin lamellae can occur in one grain (Figure 8b). Generally, the twin density is exceptionally high with $>1/\mu m$ (Figures 7 and 8), indicating high differential stresses on the order of 1 GPa.

- The crystallographic relationship between crosscutting *e*- and *r*-twins (Figure 5) as well as between the host and secondary *r*-twins in primary *f*-twins (Figure 6) is characterized by a misorientation of $35 \pm 10°$ and a misorientation axis parallel to $< 11\overline{2}0 >$. The interaction between *r*-twins with primary *f*-twins can result in so-called *a*-type lamellae, which were recently reported from high strain experiments (Schuster et al., 2020) and hitherto unknown from naturally deformed rocks.
- Calcite twinning took place controlled by the high differential stresses during quasi-instantaneous loading to relatively low shock conditions (<7 GPa shock pressure, as quartz does not contain planar deformation features).
- Deformation led to mobilization of calcite cementing the cataclasites without the involvement of melting or devolatilization.
- New grains formed after deformation by strain-induced grain boundary migration (Figure 4d,e), growth from strongly damaged crystals (Figure 9), rotation due to interaction of different twin lamellae (Figures 8c,e,f, 9 and 10), and/or precipitation from a pore fluid associated with chemical gradients (especially Langenmühle samples, Figure 4a–e).

Our study substantiates that calcite is an efficient shock barometer at relatively low shock conditions. The deviatoric component of the shock-related stress is the controlling factor and not the quasi-instantaneous loading to dynamic shock pressures, as indicated by similar calcite twin microstructures from tectonic deformation experiments. We suggest that the conditions of high differential stresses and high confining pressures both on the order of one to few GPa are required for such a twinned calcite microstructure. Thus, it might in principle also be expected in carbonate-rich fault rocks deformed coseismically at high stresses and depths where the lithostatic pressure is sufficient to prevent dominantly brittle behavior, that is, at hypocentral depths and below, which, however, has not been observed so far.

Data Availability Statement—The data that support the findings of this study are available from the corresponding author upon reasonable request.

Editorial Handling—Dr. Michael H. Poelchau

REFERENCES

Abadian, M. 1972. Petrographie, Stosswellenmetamorphose und Entstehung polymikter kristalliner Breccien im Nördlinger Ries. *Contributions to Mineralogy and Petrology* 35: 245–262. https://doi.org/10.1007/BF00371219.

Arboit, F., Amrouch, K., Collins, A. S., King, R., and Morley, C. 2015. Determination of the Tectonic Evolution from Fractures, Faults, and Calcite Twins on the Southwestern Margin of the Indochina Block. *Tectonics* 34: 1576–99. https://doi.org/10.1002/2015TC003876.

Arp, G., Dunkl, I., Jung, D., Karius, V., Lukács, R., Zeng, L., Reimer, A., and Head, J. W., III. 2021. A Volcanic Ash Layer in the Nördlinger Ries Impact Structure (Miocene, Germany): Indication of Crater Fill Geometry and Origins of Long-Term Crater Floor Sagging. *Journal of Geophysical Research: Planets* 126: e2020JE006764. https://doi.org/10.1029/2020JE006764.

Arp, G., Reimer, A., Simon, K., Sturm, S., Wilk, J., Kruppa, C., Hecht, L., et al. 2019. The Erbisberg Drilling 2011: Implications for the Structure and Postimpact Evolution of the Inner Ring of the Ries Impact Crater. *Meteoritics & Planetary Science* 54: 2448–82. https://doi.org/10.1111/maps.13293.

Barber, D. J., and Wenk, H. R. 1979. Deformation Twinning in Calcite, Dolomite, and Other Rhombohedral Carbonates. *Physics and Chemistry of Minerals* 5: 141–165. https://doi.org/10.1007/BF00307550.

Burkhard, M. 1993. Calcite Twins, their Geometry, Appearance and Significance as Stress-Strain Markers and Indicators of Tectonic Regime: A Review. *Journal of Structural Geology* 15: 351–368. https://doi.org/10.1016/0191-8141(93)90132-T.

Burt, J. B., Pope, M. C., and Watkinson, A. J. 2005. Petrographic, X-Ray Diffraction, and Electron Spin Resonance Analysis of Deformed Calcite: Meteor Crater, Arizona. *Meteoritics & Planetary Science* 40: 297–306. https://doi.org/10.1111/j.1945-5100.2005.tb00381.

Covey-Crump, S. J., Schofield, P. F., and Oliver, E. C. 2017. Using Neutron Diffraction to Examine the Onset of Mechanical Twinning in Calcite Rocks. *Journal of Structural Geology* 100: 77–97. https://doi.org/10.1016/j.jsg.2017.05.009.

Craddock, J. P., Nuriel, P., Kylander-Clark, A. R., Hacker, B. R., Luczaj, J., and Weinberger, R. 2022. Long-Term (7 Ma) Strain Fluctuations within the Dead Sea Transform System from High-Resolution U-Pb Dating of a Calcite Vein. *Geological Society of America Bulletin* 134: 1231–46. https://doi.org/10.1130/B36000.1.

De Bresser, J. H. P., and Spiers, C. J. 1993. Slip Systems in Calcite Single Crystals Deformed at 300–800°C. *Journal of Geophysical Research: Solid Earth* 98(B4): 6397–6409. https://doi.org/10.1029/92JB02044.

De Bresser, J. H. P., and Spiers, C. J. 1997. Strength Characteristics of the *r*, *f*, and *c* Slip Systems in Calcite. *Tectonophysics* 272: 1–23. https://doi.org/10.1016/S0040-1951(96)00273-9.

Dobrică, E., Ohtaki, K. K., and Engrand, C. 2022. Dolomites in Hydrated Fine-Grained Antarctic Micrometeorites: Effective Tools for Analyzing Secondary Processes. *Geochimica et Cosmochimica Acta* 317: 286–305. https://doi.org/10.1016/j.gca.2021.11.018.

Erickson, T. M., Pearce, M. A., Reddy, S. M., Timms, N. E., Cavosie, A. J., Bourdet, J., Rickard, W. D. A., and Nemchin, A. A. 2017. Microstructural Constraints on the Mechanisms of the Transformation to Reidite in Naturally Shocked Zircon. *Contributions to Mineralogy and Petrology* 172: 6. https://doi.org/10.1007/s00410-016-1322-0.

Ferrill, D. A., Morris, A. P., Evans, M. A., Burkhard, M., Groshong, R. H., Jr., and Onasch, C. M. 2004. Calcite Twin Morphology: A Low-Temperature Deformation Geothermometer. *Journal of Structural Geology* 26: 1521–29. https://doi.org/10.1016/j.jsg.2003.11.028.

Grady, M. M., Wright, I. P., Swart, P. K., and Pillinger, C. T. 1988. The Carbon and Oxygen Isotopic Composition of Meteoritic Carbonates. *Geochimica et Cosmochimica Acta* 52: 2855–66. https://doi.org/10.1016/0016-7037(88)90152-4.

Graup, G. 1977. Petrography of the Basement Rocks from the Borehole Nördlingen 1973. *Geologica Bavarica* 75: 219–230.

Graup, G. 1978. *Das Kristallin im Nördlinger Ries. Petrographische Zusammensetzung und Auswurfsmechanismus der kristallinen Trümmermassen, Struktur des kristallinen Untergrundes und Beziehungen zum Moldanubikum.* Stuttgart, Germany: Ferdinand Enke Verlag. 190 p.

Graup, G. 1999. Carbonate-Silicate Liquid Immiscibility upon Impact Melting: Ries Crater, Germany. *Meteoritics & Planetary Science* 34: 425–438. https://doi.org/10.1111/j.1945-5100.1999.tb01351.x.

Groshong, R. H., Jr. 1972. Strain Calculated from Twinning in Calcite. *Geological Society of America Bulletin* 83: 2025–38. https://doi.org/10.1130/0016-7606(1972)83[2025:SCFTIC]2.0.CO;2.

Hirth, J. P., and Lothe, J. 1982. *Theory of Dislocations.* New York: John Wiley, 857 pp. https://doi.org/10.1115/1.3167075.

Hörz, F., Ostertag, R., and Rainey, D. A. 1983. Bunte Breccia of the Ries: Continuous Deposit of Large Impact Craters. *Reviews of Geophysics and Space Physics* 21: 1667–1725. https://doi.org/10.1029/RG021i008p01667.

Hough, R., Gilmour, I., Pillinger, C., Arden, J. W., Gilkess, K. W. R., Yuan, J., and Milledge, H. J. 1995. Diamond and Silicon Carbide in Impact Melt Rock from the Ries Impact Crater. *Nature* 378: 41–44. https://doi.org/10.1038/378041a0.

Hüttner, R. 1977. Macroscopic Observations on the Deformation of the Crystalline Rocks from the Borehole Nördlingen 1973. *Geologica Bavarica* 75: 273–284.

Hüttner, R., and Schmidt-Kaler, H. 1999. Die Geologische Karte des Rieses 1: 50 000 (2., überarbeitete Auflage). *Geologica Bavarica* 104: 7–76.

Kaplan, H. H., Lauretta, D. S., Simon, A. A., Hamilton, V. E., DellaGiustina, D. N., Golish, D. R., Reuter, D. C., et al. 2020. Bright Carbonate Veins on Asteroid (101955) Bennu: Implications for Aqueous Alteration History. *Science* 370: eabc3557. https://doi.org/10.1126/science.abc3557.

Kenkmann, T., Winkler, R., Poelchau, M. H., Wirth, R., Luther, R., and Schaefer, F. 2018. Impact-Induced Twinning in Calcite as Revealed by MEMIN Experiments with Marble. *81st Annual Meeting of the Meteoritical Society*, vol. 81, abstract # 2067, p. 6147.

Kurosawa, K., Genda, H., Azuma, S., and Okazaki, K. 2021. The Role of Post-Shock Heating by Plastic Deformation during Impact Devolatilization of Calcite ($CaCO_3$). *Geophysical Research Letters* 48: 1–9. https://doi.org/10.1029/2020GL091130.

Kurosawa, K., Ono, H., Niihara, T., Sakaiya, T., Kondo, T., Tomioka, N., Mikouchi, T., et al. 2022. Shock Recovery with Decaying Compressive Pulses: Shock Effects in Calcite ($CaCO_3$) around the Hugoniot Elastic Limit. *Journal of Geophysical Research: Planets* 127: 1–15. https://doi.org/10.1029/2021JE007133.

Lacombe, O. 2007. Comparison of Paleostress Magnitudes from Calcite Twins with Contemporary Stress Magnitudes and Frictional Sliding Criteria in the Continental Crust: Mechanical Implications. *Journal of Structural Geology* 29: 86–99. https://doi.org/10.1016/j.jsg.2006.08.009.

Langenhorst, F., Boustie, M., Deutsch, A., Hornemann, U., Matignon, C., Migault, A., and Romain, J. P. 2003. Experimental Techniques for the Simulation of Shock Metamorphism: A Case Study on Calcite. In *High-Pressure Shock Compression of Solids V*, 1–27. New York: Springer.

Lee, M. R., Lindgren, P., and Sofe, M. R. 2014. Aragonite, Breunnerite, Calcite and Dolomite in the CM Carbonaceous Chondrites: High Fidelity Recorders of Progressive Parent Body Aqueous Alteration. *Geochimica et Cosmochimica Acta* 144: 126–156. https://doi.org/10.1016/j.gca.2014.08.019.

Lindgren, P., Lee, M. R., Sofe, M., and Burchell, M. J. 2011. Microstructure of Calcite in the CM2 Carbonaceous Chondrite LON 94101: Implications for Deformation History during and/or after Aqueous Alteration. *Earth and Planetary Science Letters* 306: 289–298. https://doi.org/10.1016/j.epsl.2011.04.022.

Lindgren, P., Price, M. C., Lee, M. R., and Burchell, M. J. 2013. Constraining the Pressure Threshold of Impact Induced Calcite Twinning: Implications for the Deformation History of Aqueously Altered Carbonaceous Chondrite Parent Bodies. *Earth and Planetary Science Letters* 384: 71–80. https://doi.org/10.1016/j.epsl.2013.10.002.

Melosh, H. J. 1989. *Impact Cratering: A Geologic Process.* New York: Oxford University Press, 245 p.

Niles, P. B., Catling, D. C., Berger, G., Chassefière, E., Ehlmann, B. L., Michalski, J. R., Morris, R., Ruff, S. W., and Sutter, B. 2013. Geochemistry of Carbonates on Mars: Implications for Climate History and Nature of Aqueous Environments. *Space Science Reviews* 174: 301–328. https://doi.org/10.1007/s11214-012-9940-y.

Osinski, G. R. 2003. Impact Glasses in Fallout Suevites from the Ries Impact Structure, Germany: An Analytical SEM Study. *Meteoritics & Planetary Science* 38: 1641–67. https://doi.org/10.1111/j.1945-5100.2003.tb00006.xsk.

Parlangeau, C., Dimanov, A., Lacombe, O., Hallais, S., and Daniel, J. M. 2019. Uniaxial Compression of Calcite Single Crystals at Room Temperature: Insights into Twinning Activation and Development. *Solid Earth* 10: 307–316. https://doi.org/10.5194/se-10-307-2019.

Pohl, J., Stöffler, D., Gall, H., and Ernston, K. 1977. The Ries Impact Crater. In *Impact and Explosion Cratering*, edited by D. J. Roddy, R. O. Pepin, and R. B. Merrill, 343–404. New York: Pergamon Press.

Rae, A. S. P., Collins, G., Poelchau, M. H., Riller, U., Davison, T. M., Grieve, R. A. F., Osinski, G. R., Morgan, J. V., and IODP-ICDP Expedition 364 Scientists. 2019. Stress-Strain Evolution during Peak-Ring Formation: A Case Study of the Chicxulub Impact Structure. *Journal of Geophysical Research: Planets* 124: 396–417. https://doi.org/10.1029/2018JE005821.

Rae, A. S. P., Poelchau, M. H., and Kenkman, T. 2021. Stress and Strain during Shock Metamorphism. *Icarus* 370: 114687. https://doi.org/10.1016/j.icarus.2021.114687.

Rocholl, A., Böhme, M., Gilg, H. A., Pohl, J., Schaltegger, U., and Wijbrans, J. 2018. Comment on "A High-Precision $^{40}Ar/^{39}Ar$ Age for the Nördlinger Ries Impact Crater, Germany, and Implications for the Accurate Dating of Terrestrial Impact Events" by Schmieder et al. (Geochim. Cosmochim. Acta 220 (2018) 146–157). *Geochimica et Cosmochimica Acta* 238: 599–601. https://doi.org/10.1016/j.gca.2018.05.018.

Rocholl, A., Schaltegger, U., Gilg, H. A., Wijbrans, J., and Böhme, M. 2018. The Age of Volcanic Tuffs from the Upper Freshwater Molasse (North Alpine Foreland Basin) and their Possible Use for Tephrostratigraphic Correlations across Europe for the Middle Miocene. *International Journal of Earth Sciences* 107: 387–407. https://doi.org/10.1007/s00531-017-1499-0.

Rowe, K. J., and Rutter, E. H. 1990. Palaeostress Estimation Using Calcite Twinning: Experimental Calibration and Application to Nature. *Journal of Structural Geology* 12: 1–17. https://doi.org/10.1016/0191-8141(90)90044-Y.

Rybacki, E., Evans, B., Janssen, C., Wirth, R., and Dresen, G. 2013. Influence of Stress, Temperature, and Strain on Calcite Twins Constrained by Deformation Experiments. *Tectonophysics* 601: 20–36. https://doi.org/10.1016/j.tecto.2013.04.021.

Rybacki, E., Niu, L., and Evans, B. 2021. Semi-Brittle Deformation of Carrara Marble: Hardening and Twinning Induced Plasticity. *Journal of Geophysical Research: Solid Earth* 126: e2021JB022573. https://doi.org/10.1029/2021JB022573.

Schmieder, M., Kennedy, T., Jourdan, F., Buchner, E., and Reimold, W. U. 2018a. A High-Precision $^{40}Ar/^{39}Ar$ Age for the Nördlinger Ries Impact Crater, Germany, and Implications for the Accurate Dating of Terrestrial Impact Events. *Geochimica et Cosmochimica Acta* 220: 146–157. https://doi.org/10.1016/j.gca.2017.09.036.

Schmieder, M., Kennedy, T., Jourdan, F., Buchner, E., and Reimold, W. U. 2018b. Response to Comment on "A High-Precision $^{40}Ar/^{39}Ar$ Age for the Nördlinger Ries Impact Crater, Germany, and Implications for the Accurate Dating of Terrestrial Impact Events" by Schmieder Et al. (Geochim. Cosmochim. Acta 220 (2018) 146–157). *Geochimica et Cosmochimica Acta* 238: 602–5. https://doi.org/10.1016/j.gca.2018.07.025.

Schuster, R., Habler, G., Schafler, E., and Abart, R. 2020. Intragranular Deformation Mechanisms in Calcite Deformed by High-Pressure Torsion at Room Temperature. *Mineralogy and Petrology* 114: 105–118. https://doi.org/10.1007/s00710-019-00690-y.

Schwarz, W. H., Hanel, M., and Trieloff, M. 2020. U-Pb Dating of Zircons from an Impact Melt of the Nördlinger Ries Crater. *Meteoritics & Planetary Science* 55: 312–325. https://doi.org/10.1111/maps.13437.

Skála, R. 2002. Shock-Induced Phenomena in Limestones in the Quarry near Ronheim, Ries Crater, Germany. *Bulletin of the Czech Geological Survey* 77: 313–320.

Stähle, V., Altherr, R., Koch, M., and Nasdala, L. 2008. Shock Induced Growth and Metastability of Stishovite and Coesite in Lithic Clasts from Suevite of the Ries Impact Crater (Germany). *Contributions to Mineralogy and Petrology* 155: 457–472.

Stähle, V., and Otteman, J. 1977. Zeolithization of Glass in the Suevite and Petrography of the Fallback Suevite and the Dike Breccias (Borehole Nördlingen 1973). *Geologica Bavarica* 75: 191–218.

Stöffler, D., Artemieva, N. A., Wünnemann, K., Reimold, W. U., Jacob, J., Hansen, B. K., and Summerson, I. A. 2013. Ries Crater and Suevite Revisited—Observations and Modeling Part I: Observations. *Meteoritics & Planetary Science* 48: 515–589. https://doi.org/10.1111/maps.12086.

Stöffler, D., Ewald, U., Ostertag, R., and Reimold, W. U. 1977. Research Drilling Nordlingen 1973 (Ries) Composition and Texture of Polymict Impact Breccias. *Geologica Bavarica* 75: 163–190.

Stöffler, D., Hamann, C., and Metzler, K. 2018. Shock Metamorphism of Planetary Silicate Rocks and Sediments: Proposal for an Updated Classification System. *Meteoritics & Planetary Science* 53: 5–49. https://doi.org/10.1111/maps.12912.

Sturm, S., Kenkmann, T., Willmes, M., Pösges, G., and Hiesinger, H. 2015. The Distribution of Megablocks in the Ries Crater, Germany: Remote Sensing, Field Investigation, and Statistical Analyses. *Meteoritics & Planetary Science* 50: 141–171. https://doi.org/10.1111/maps.12408.

Trepmann, C. A. 2008. Shock Effects in Quartz: Compression Versus Shear Deformation—An Example from the Rochechouart Impact Structure, France. *Earth and Planetary Science Letters* 267: 322–332. https://doi.org/10.1016/j.epsl.2007.11.035.

Von Engelhardt, W. 1990. Distribution, Petrography and Shock Metamorphism of the Ejecta of the Ries Crater in Germany—A Review. *Tectonophysics* 171: 259–273. https://doi.org/10.1016/0040-1951(90)90104-G.

Von Engelhardt, W. 1997. Suevite Breccia of the Ries Impact Crater, Germany: Petrography, Chemistry and Shock Metamorphism of Crystalline Rock Clasts. *Meteoritics & Planetary Science* 32: 545–554. https://doi.org/10.1111/j.1945-5100.1997.tb01299.x.

Von Engelhardt, W., and Graup, G. 1984. Suevite of the Ries Crater, Germany: Source Rocks and Implications for Cratering Mechanics. *Geologische Rundschau* 73: 447–481.

Wheeler, J., Prior, D., Jiang, Z., Spiess, R., and Trimby, P. 2001. The Petrological Significance of Misorientations between Grains. *Contributions to Mineralogy and Petrology* 141: 109–e124.

Wünnemann, K., Morgan, J. V., and Jödicke, H. 2005. Is Ries Crater Typical for its Size? An Analysis Based upon Old and New Geophysical Data and Numerical Modeling. *Large Meteorite Impacts III*, vol. 384, 67–83. https://doi.org/10.1130/0-8137-2384-1.67.